Journal of Research in Health Sciences
ISSN: 2228-7809 | https://jrhsjournal.com

# Upscaling clinical measurements from controlled conditions to real-world patient data using a physiology-based method

**Dr. H. Zhang[1], Dr. Y. Lin[2]***

[1] School of Preventive Medicine and Environmental Health, Peking University Health Science Center, Beijing 100191, China
[2] Institute of Health Data Science and Biomedical Engineering, Fudan University, Shanghai 200032, China

## 1. Background

Solar-induced chlorophyll fluorescence (SIF) is closely linked to photosynthesis, and provides new opportunities for detecting global Gross Primary Production (GPP). Instantaneous satellite SIF products are usually available only for clear-sky condition, which means that there is a temporal inconsistency in the direct link between these and continuous carbon flux records. Therefore, the temporally sparse nature of satellite SIF products has limited the use of SIF in GPP estimation.

Several studies (Frankenberg et al., 2011; Joiner et al., 2016) upscaled the instantaneous SIF to daily sums using the clear-sky irradiance (the cosine of the solar zenith angle, cos(SZA)) as a proxy so as to reduce the variability in SIF–GPP correlations caused by changes in latitude and season. However, this approach failed to eliminate the effects of changes in weather conditions (Hu et al., 2018). Obviously, the CSSIF products were applicable only for clear-sky conditions and cannot be used to derive all-sky sums of photosynthetic capacity for a continuous period. The temporal mismatch between clear-sky satellite-based SIF and GPP remains an obstacle to a better understanding of the SIF–GPP relationship and the monitoring of global GPP.

To address this issue, we designed an APAR-based method to upscale the GOME-2 SIF (developed by Joiner et al., 2016) from instantaneous clear-sky observations to all-sky sums, and hereby derived a SIF product for all-sky conditions (ASSIF) from GOME-2 at 8-day and monthly intervals during 2007 and 2018. The SIF all-sky upscaling method was generated with several explanatory variables, including instantaneous GOME-2 soundings, MODIS vegetation indices, and the photosynthetically active radiation (PAR) from the Modern-Era Retrospective Analysis for Research and Applications Version 2 (Merra-2). A global 0.5-degree ASSIF product was produced for 2007–2018 at 8-day and monthly intervals was introduced and shared here.

## 2. Upscaling clear-sky SIF to all-sky sums

SIF is a directly emitted part of the absorbed photosynthetically active radiation. Similar to the light-use efficiency (LUE) concept for photosynthesis, the SIF can be expressed as follows (Berry et al., 2012; Guanter et al., 2014):

$$\mathrm{SIF} = \mathrm{APAR} \times \mathrm{LUE_f} = \mathrm{APAR} \times \Phi_{\mathrm{SIF}} \times \varepsilon \quad (1)$$

where $\mathrm{LUE_f}$ is the effective light-use efficiency of the canopy fluorescence, which is a product of the fluorescence quantum yield ($\Phi_{\mathrm{SIF}}$) and the fraction of SIF photons escaping from the photosystem level to the canopy level ($\varepsilon$).

Then, the average of instantaneous SIF retrievals ($\overline{\mathrm{SIF_{ins}}}$) and the average of all-sky SIF values ($\overline{\mathrm{SIF_{all}}}$) can be respectively formulated as:

$$\overline{\mathrm{SIF_{ins}}} = \sum \mathrm{PAR_{ins}} \times \mathrm{FAPAR_{ins}} \times \Phi_{\mathrm{SIF_{ins}}} \times \varepsilon_{\mathrm{ins}}/N \quad (2)$$

$$\overline{\mathrm{SIF_{all}}} = \sum \mathrm{PAR_{all}} \times \mathrm{FAPAR_{all}} \times \Phi_{\mathrm{SIF_{all}}} \times \varepsilon_{\mathrm{all}}/NN \quad (3)$$

where the subscript 'ins' represents the instantaneous moments for clear-sky SIF retrievals and the subscript 'all' represents the continuous moments for all-sky conditions. The time window for satellite-based SIF averaging is usually 8-day or monthly period, in which $N$ is the number of instantaneous valid retrievals and $NN$ is the number of all continuous moments during the averaging time window (e.g. for 8-day period, it can be set to 192 for one-hour interval). Accordingly, the upscaling factor from instantaneous SIF to all-sky SIF can be calculated as

$$\frac{\overline{\mathrm{SIF_{all}}}}{\overline{\mathrm{SIF_{ins}}}} = \frac{\sum \mathrm{PAR_{all}} \times \mathrm{FAPAR_{all}} \times \Phi_{\mathrm{SIF_{all}}} \times \varepsilon_{\mathrm{all}}/NN}{\sum \mathrm{PAR_{ins}} \times \mathrm{FAPAR_{ins}} \times \Phi_{\mathrm{SIF_{ins}}} \times \varepsilon_{\mathrm{ins}}/N} \quad (4)$$

Among the three terms on the right-hand side of Equation (1), APAR has been proved to be the dominate factor affecting the diurnal and seasonal variations of SIF. Many ground-based studies (Yang et al., 2015; Yang, et al., 2018; Hu et al., 2018) have observed a highly linear correlation between APAR and far-red SIF with an $R^2$ larger than 0.8 during the growing season of the temperate deciduous forest, rice, or maize. According to the theoretical and modelling

analysis in Yang and Van der Tol (2018), the seasonal variations in $LUE_f$ is dominated by the fraction of SIF escaping the canopy (i.e. $\varepsilon$), which can be mainly affected by the canopy structure, the pigments, and the incident and observed geometries. With the quantitative simulated and in-situ experiments, Du et al. (2017) found that for an invariable plant type (e.g. planophile or erectophile), the $LUE_f$ has very conservative variation with different chlorophyll content, vegetation cover, and solar zenith angle. The fraction of diffuse radiation is more reported to significantly affect the LUE of photosynthesis ($LUE_p$) than the $LUE_f$, due to the light saturate of photosynthesis for sunlit leaves (Gu et al., 2002; Zhang et al, 2020). And the $LUE_p$ changes with a range of an order of magnitude greater compared to the change of $LUE_f$ (Damm et al., 2015, Yang et al., 2015). In addition, according to the mechanistic light response function and leaf-scale experiments in Gu et al., (2019), $\Phi_{SIF}$ has a relatively muted sensitivity to variations in environmental conditions like light level and temperature due to the compensate effects of the fraction of open PSII reaction centers (qL) and the non-photochemical quenching (NPQ). The effect of clouds on APAR can be much greater than that on $LUE_f$. Therefore, in this study, within a limited temporal period when the plant's type remains invariable, we put emphasis on the differences of APAR among different weather conditions, and ignore the much lower changes in $LUE_f$. Assuming the $\Phi_{SIF}$ and $\varepsilon$ are constant during a month, Equation (4) can be simplified as:

$$\frac{\overline{SIF_{all}}}{\overline{SIF_{ins}}} = \frac{\sum PAR_{all} \times FAPAR_{all}/NN}{\sum PAR_{ins} \times FAPAR_{ins}/N} \tag{5}$$

Considering the uncertainty in the inversed variable products (i.e., FAPAR), it was replaced by a direct observed remote sensing variable. Previous studies have demonstrated that the FAPAR can be directly quantified by spectral vegetation indexes such as NDVI and EVI, and can be estimated using an VI-based linear stretching model (Sellers et al. 1994; Jiang et al. 2002; Liu et al., 2017b). According to the simulation experiment conducted by Liu et al. (2020), NDVI is significantly correlated to FAPAR with an $R^2$ of 0.914; the intercept in the NDVI-based linear regression model is very small (0.004), compared to its slope (1.008). Therefore, FAPAR in equation (5) can be replaced by NDVI. Since EVI is more sensitive to dense vegetation conditions than the NDVI (Huete et al., 2002), it was selected as a satellite-based proxy of FAPAR to denote the changing of vegetation conditions in this study. Accordingly, the all-sky SIF at both monthly ($ASSIF_{mon}$) and 8-day ($ASSIF_{8d}$) intervals can be upscaled from instantaneous clear-sky SIF by as follows:

$$\begin{cases} ASSIF_{mon} = \begin{cases} \sum_{mon}^{M} SIF_{ins} \cdot \frac{\overline{PAR_{mon}} \cdot \overline{VI_{mon}}}{\sum_{mon}^{M} PAR_{ins} VI_{ins}} & if\ \overline{VI_{mon}} \geq 0.2 \\ \sum_{mon}^{M} SIF_{ins} \cdot \frac{\overline{PAR_{mon}}}{\sum_{mon}^{M} PAR_{ins}} & if\ \overline{VI_{mon}} < 0.2 \end{cases} \\ ASSIF_{8d} = \begin{cases} \sum_{8d}^{D} SIF_{ins} \cdot \frac{\overline{PAR_{8d}}}{\sum_{8d}^{D} PAR_{ins}} & if\ D > D_0 \\ \left.\begin{cases} \sum_{mon}^{M} SIF_{ins} \cdot \frac{\overline{PAR_{8d}} \cdot \overline{VI_{8d}}}{\sum_{mon}^{M} PAR_{ins} VI_{ins}} & if\ \overline{VI_{8d}} \geq 0.2 \\ \sum_{mon}^{M} SIF_{ins} \cdot \frac{\overline{PAR_{8d}}}{\sum_{mon}^{M} PAR_{ins}} & if\ \overline{VI_{8d}} < 0.2 \end{cases}\right\} & if\ D \leq D_0 \end{cases} \end{cases} \tag{6}$$

where $SIF_{ins}$ was derived from the GOME-2 level-2 SIF datasets at clear-sky (less than 30% cloud fraction) measurement instants, $PAR_{ins}$ is the estimated PAR for these instants, derived from the Merra-2 meteorological data, and $EVI_{ins}$ is the 8-day MODIS EVI closest to these instants. *D* and *M* are the numbers of valid retrievals within each 0.5° cell during the 8-day and monthly period, respectively. Note that the time window between $\sum SIF_{ins}$ and $\sum PAR_{ins} \cdot VI_{ins}$ is the same, i.e. both during one month or both during 8 days, and the valid instants during such time window involved in the calculation of them two also keep equal.

To reduce the propagation of errors from global datasets, several rules were set during the processing of satellite SIF upscaling. First, the VI was not involved in the model if the grid cell had low vegetation coverage (i.e. the averaged EVI was less than 0.2) for the generation of ASSIF at both 8-day and monthly scales. Second, if the recorded samples of the satellite-based SIF during 8-day period is very limited, we use all the valid SIF retrievals during one-month period to determine the 8-day SIF, which will decrease the uncertainties resulted from the noised SIF signals. For the generation of 8-day ASSIF, if *D* was larger than the threshold ($D_0$), the time window for the averaging of $SIF_{ins}$ values was set to 8 days, and correspondingly, the time window for the averaging of $\sum PAR_{ins} \cdot VI_{ins}$. In this way, the VI terms in the numerator and denominator cancel out (see the third fraction of Equation (6)), since 8-day EVI was used in the model by ignoring the variation of EVI within such time scale. Otherwise, the time window for the averaging of $SIF_{ins}$ values was extended to a month, in order to compromise the errors from limited SIF retrievals during 8 days. Based on our test made with the 2007–2018 GOME-2 datasets, the values of *M* and *D* change a lot across different latitudes with the mean

of about 15 (5) and the maximum of nearly 100 (50), respectively. The threshold $D_0$ was set to 5 to satisfy the needs of both smoothness and validity.

### 3. Spatial comparison among different SIF products

Three 8-day and monthly SIF products were generated in this work, including the original averaged SIF (OSIF), which was produced by simple mathematical averaging, and the clear-sky upscaled SIF (CSSIF) (Frankenberg et al., 2011; Joiner et al., 2016) and ASSIF, which were generated based on Equation (4). We first compared the spatial distribution of the 8-day SIF products: Fig. 1 displays the spatial distribution of $OSIF_{8d}$ and $ASSIF_{8d}$ for two 8-day periods (the 137$^{th}$ day in 2007 and the 225$^{th}$ day in 2014). The negative 8-day SIF values were excluded in the map. It is obvious that the $ASSIF_{8d}$ products can fill the spatial gaps in the current $OSIF_{8d}$ because the temporal window has been extended from 8 days to one month for grid cells that do not have valid SIF soundings during the relevant 8-day period.

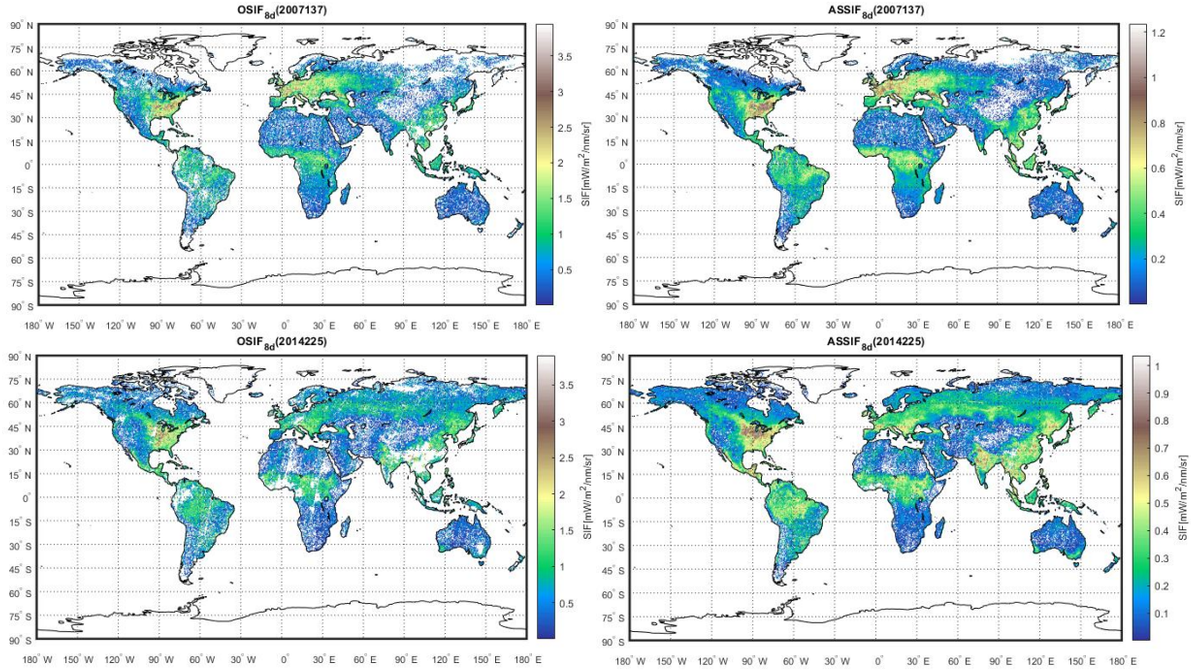


**Fig. 6.** Spatial distribution of the $OSIF_{8d}$ (a,c) and $ASSIF_{8d}$ (b,d) for the 137$^{th}$ day in 2007 and the 225$^{th}$ day in 2014

To analyze the differences between CSSIF and ASSIF across the globe, we then calculated the adjusted relative difference, $a\_REsif_{year}$, between $CSSIF_{year}$ and $ASSIF_{year}$, as well as the absolute difference between them two (ΔSIF). Fig. 2 shows ΔSIF and $a\_REsif_{year}$ for 2010 along with the cloudiness index map for the year. The negative yearly SIF values were excluded in the SIF map. In general, CSSIF is higher than ASSIF for most grid cells across the globe, producing a ΔSIF from -0.051 to 0.135 mW/m$^2$/nm/sr. The ΔSIF values were positive for most grid cells, especially for humid regions. But due to the occasional SIF retrievals made on cloudy days, a few negative ΔSIF values also exist. More importantly, the global $a\_REsif_{year}$ and ΔSIF map has a similar spatial distribution to the annual CloudI map. In particular, the overestimation in CSSIF compared with ASSIF is more obvious for more humid regions where the cloudiness index is larger than 0.5.

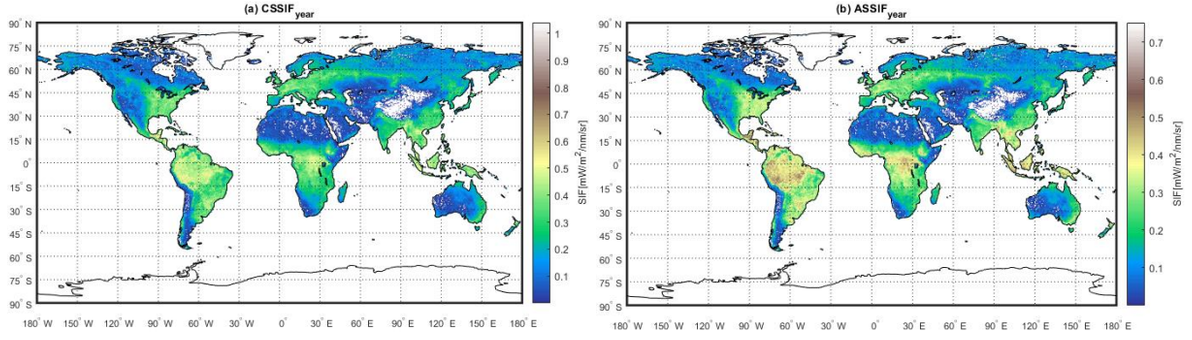

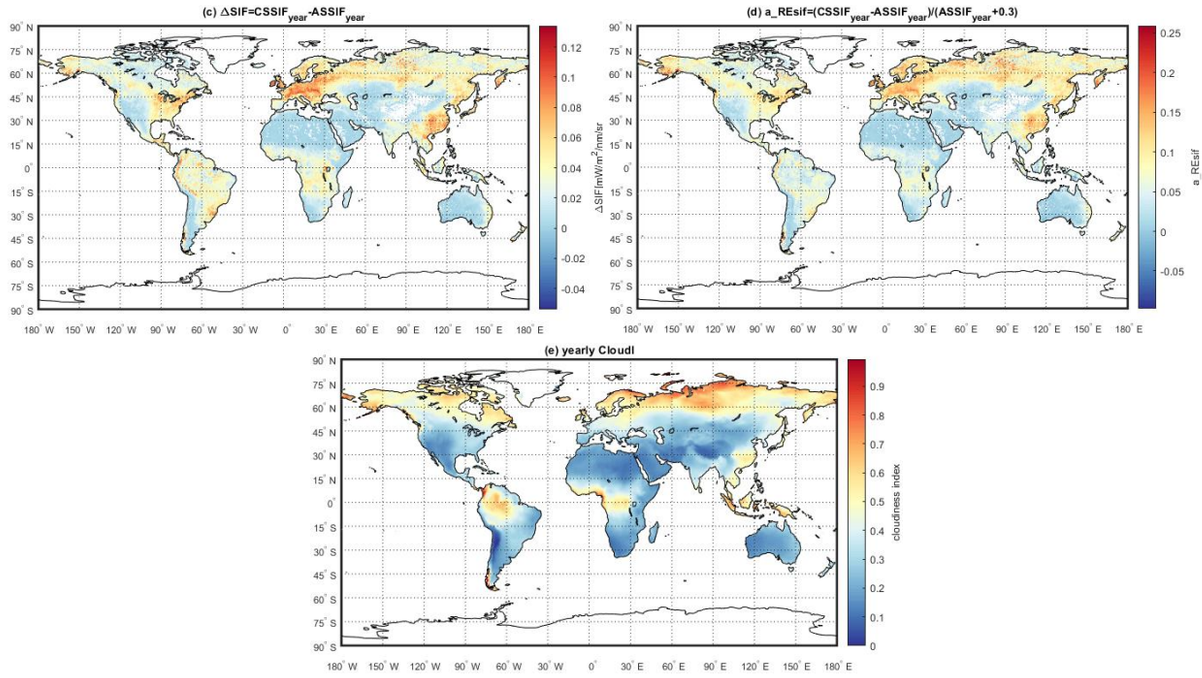


**Fig. 2**. Spatial differences between ASSIF$_{year}$ and CSSIF$_{year}$ products for 2010, with the map of the cloudiness index shown for comparison

**4. Acknowledgments**

This work was supported by the Key Research Program of the Chinese Academy of Sciences (ZDRW-ZS-2019-1), and the National Natural Science Foundation of China, grant number 41825002.

**5. References**

Berry, J.A., Frankenberg, C., Wennberg, P., Baker, I., Bowman, K.W., Castro-Contreas, S., Cendrero-Mateo, M.P., Damm, A., Drewry, D., Ehlmann, B., 2012. New methods for measurement of photosynthesis from space. Geophys. Res. Lett. 38, L17706.

Damm, A., Guanter, L., Paul-Limoges, E., van der Tol, C., Hueni, A., Buchmann, N., Eugster, W., Ammann, C., Schaepman, M.E., 2015. Far-red sun-induced chlorophyll fluorescence shows ecosystem-specific relationships to gross primary production: an assessment based on observational and modeling approaches. Remote Sens. Environ. 166, 91–105.

Du, S., Liu, L., Liu, X., Hu, J., 2017. Response of canopy solar-induced chlorophyll fluorescence to the absorbed photosynthetically active radiation absorbed by chlorophyll. Remote Sensing 9 (9), 911.

Frankenberg, C., Fisher, J.B., Worden, J., Badgley, G., Saatchi, S.S., Lee, J.-E., Toon, G.C., Butz, A., Jung, M., Kuze, A., Yokota, T., 2011. New global observations of the terrestrial carbon cycle from GOSAT: patterns of plant fluorescence with gross primary productivity. Geophys. Res. Lett. 38 (17).

Frankenberg, C., O'Dell, C., Berry, J., Guanter, L., Joiner, J., Köhler, P., Pollock, R., Taylor, T.E., 2014. Prospects for chlorophyll fluorescence remote sensing from the Orbiting Carbon Observatory-2. Remote Sens. Environ. 147, 1–12.

Friedl, M. A., Sulla-Menashe, D., Tan, B., Schneider, A., Ramankutty, N., Sibley, A., Huang, X., 2010. MODIS Collection 5 global land cover: Algorithm refinements and characterization of new datasets. Remote sensing of Environment 114 (1), 168–182.

Gelaro, R., McCarty, W., Suárez, M.J., Todling, R., Molod, A., Takacs, L., ... & Wargan, K., 2017. The modern-era retrospective analysis for research and applications, version 2 (MERRA-2). Journal of Climate 30 (14), 5419–5454.

Gentine, P., Alemohammad, S. H., 2018. Reconstructed solar-induced fluorescence: A machine learning vegetation product based on MODIS surface reflectance to reproduce GOME-2 solar-induced fluorescence. Geophysical research letters 45 (7), 3136–3146.

Gu, L., Han, J., Wood, J. D., Chang, C. Y. Y., Sun, Y., 2019. Sun-induced Chl fluorescence and its importance for biophysical modeling of photosynthesis based on light reactions. New Phytologist.

Guan, K., Berry, J. A., Zhang, Y., Joiner, J., Guanter, L., Badgley, G., & Lobell, D. B., 2016. Improving the monitoring of crop productivity using spaceborne solar-induced fluorescence. Global change biology 22 (2), 716–726.

Guanter, L., Frankenberg, C., Dudhia, A., Lewis, P.E., Gómez-Dans, J., Kuze, A., Suto, H., Grainger, R.G., 2012. Retrieval and global assessment of terrestrial chlorophyll fluorescence from GOSAT space measurements. Remote Sens. Environ. 121, 236–251.

Guanter, L., Zhang, Y., Jung, M., Joiner, J., Voigt, M., Berry, J.A., Frankenberg, C., Huete, A.R., Zarco-Tejada, P., Lee, J.-E., 2014a. Global and time-resolved monitoring of crop photosynthesis with chlorophyll fluorescence. Proc. Natl. Acad. Sci. U. S. A. 111 (14), E1327–E1333.

Guanter, L., Zhang, Y., Jung, M., Joiner, J., Voigt, M., Berry, J.A., Frankenberg, C., Huete, A.R., Zarco-Tejada, P., Lee, J.-E., 2014b. Reply to Magnani et al.: linking large-scale chlorophyll fluorescence observations with cropland gross primary production. Proc. Natl. Acad. Sci. U. S. A. 111 (25), E2511–E2511.

Hu, J., Liu, L., Guo, J., Du, S., Liu, X., 2018. Upscaling Solar-Induced Chlorophyll Fluorescence from an Instantaneous to Daily Scale Gives an Improved Estimation of the Gross Primary Productivity. Remote Sensing 10 (10), 1663.

Huete, A., Didan, K., Miura, T., Rodriguez, E. P., Gao, X., Ferreira, L. G., 2002. Overview of the radiometric and biophysical performance of the MODIS vegetation indices. Remote sensing of environment 83 (1-2), 195–213.

Jiang, D., Wang, N., Yang, X., Liu, H., 2002. Dynamic properties of absorbed photosynthetic active eadiation and its relation to crop yield. Syst. Sciemces Compr. Stud. Agric. 18 (1), 51–54.

Joiner, J., Yoshida, Y., Vasilkov, A.P., Corp, L.A., Middleton, E.M., 2011. First observations of global and seasonal terrestrial chlorophyll fluorescence from space. Biogeosciences 8 (3), 637–651.

Joiner, J., Guanter, L., Lindstrot, R., Voigt, M., Vasilkov, A.P., Middleton, E.M., Huemmrich, K.F., Yoshida, Y., Frankenberg, C., 2013. Global monitoring of terrestrial chlorophyll fluorescence from moderate spectral resolution near-infrared satellite measurements: methodology, simulations, and application to GOME-2. Atmos. Meas. Tech. 6 (10), 2803–2823.

Joiner, J., Yoshida, Y., Guanter, L., Middleton, E.M., 2016. New methods for the retrieval of chlorophyll red fluorescence from hyperspectral satellite instruments: simulations and application to GOME-2 and SCIAMACHY. Atmos. Meas. Tech. 9, 3939–3967.

Köhler, P., Guanter, L., Joiner, J., 2015. A linear method for the retrieval of sun-induced chlorophyll fluorescence from GOME-2 and SCIAMACHY data. Atmos. Meas. Tech. Discuss. 8, 2589–2608.

Köhler, P., Guanter, L., Kobayashi, H., Walther, S., Yang, W., 2018a. Assessing the potential of sun-induced fluorescence and the canopy scattering coefficient to track large-scale vegetation dynamics in Amazon forests. Remote Sensing of Environment 204, 769–785.

Köhler, P., Frankenberg, C., Magney, T. S., Guanter, L., Joiner, J., & Landgraf, J., 2018b. Global retrievals of solar-induced chlorophyll fluorescence with TROPOMI: First results and intersensor comparison to OCO-2. Geophysical Research Letters 45(19), 10–456.

Li, X., Xiao, J., 2019. A Global, 0.05-Degree Product of Solar-Induced Chlorophyll Fluorescence Derived from OCO-2, MODIS, and Reanalysis Data. Remote Sensing 11 (5), 517.

Liu, L., Liu, X., Hu, J., 2015. Effects of spectral resolution and SNR on the vegetation solar-induced fluorescence retrieval using FLD-based methods at canopy level. Eur. J. Remote Sens. 48, 743–762.

Liu, L., Liu, X., Hu, J., Guan, L., 2017a. Assessing the wavelength-dependent ability of solar-induced chlorophyll fluorescence to estimate the GPP of winter wheat at the canopy level. Int. J. Remote Sens. 38, 4396–4417.

Liu, L., Guan, L., Liu, X., 2017b. Directly estimating diurnal changes in GPP for C3 and C4 crops using far-red sun-induced chlorophyll fluorescence. Agric. For. Meteorol. 232, 1–9.

Liu, L., Liu, X., Chen, J., Du, S., Ma, Y., Qian, X., Chen, S., Peng, D., 2020. Estimating Maize GPP using Near-infrared Radiance of Vegetation. Science of Remote Sensing, 100009.

Liu, S., Xu, Z., Wang, W., Jia, Z., Zhu, M., Bai, J., Wang, J., 2011. A comparison of eddy-covariance and large aperture scintillometer measurements with respect to the energy balance closure problem. Hydrol. Earth Syst. Sci. 15 (4), 1291–1306.

Liu, X., Liu, L., Hu, J., Guo, J., Du, S., 2019. Improving the potential of red SIF for estimating GPP by downscaling from the canopy level to the photosystem level. Agricultural and Forest Meteorology 281, 107846.

Magney, T. S., Bowling, D. R., Logan, B. A., Grossmann, K., Stutz, J., Blanken, P. D., ... & Lopez, S., 2019. Mechanistic evidence for tracking the seasonality of photosynthesis with solar-induced fluorescence. Proceedings of the National Academy of Sciences 116 (24), 11640–11645.

Maier, S.W., Günther, K.P., Stellmes, M., 2003. Sun-induced fluorescence: a new tool for precision farming. In: McDonald, M., Schepers, J., Tartly, L., Toai, T., Major, D. (Eds.), Digital Imaging and Spectral Techniques: Applications to Precision Agriculture and Crop Physiology. American Society of Agronomy Special Publication, Madison, WI, USA, pp. 209–222.

Myneni, R.B., Williams, D.L., 1994. On the relationship between FAPAR and NDVI. Remote Sens. Environ. 49 (3), 200–211.

Porcar-Castell, A., Tyystjärvi, E., Atherton, J., van der Tol, C., Flexas, J., Pfündel, E.E., Moreno, J., Frankenberg, C., Berry, J.A., 2014. Linking chlorophyll a fluorescence to photosynthesis for remote sensing applications: mechanisms and challenges. J. Exp. Bot. 65 (15), 4065–4095.

Porcar-Castell, A., Mac Arthur, A., Rossini, M., Eklundh, L., Pacheco-Labrador, J., Anderson, K., ... & Cerasoli, S., 2015. EUROSPEC: at the interface between remote-sensing and ecosystem $CO_2$ flux measurements in Europe. Biogeosciences 12 (20), 6103–6124.

Rahman, M.M., Lamb, D.W., Stanley, J.N., 2015. The impact of solar illumination angle when using active optical sensing of NDVI to infer fAPAR in a pasture canopy. Agric. For. Meteorol. 202, 39–43.

Reichstein, M., Falge, E., Baldocchi, D., Papale, D., Aubinet, M., Berbigier, P., ... & Grünwald, T., 2005. On the separation of net ecosystem exchange into assimilation and ecosystem respiration: review and improved algorithm. Global Change Biology 11 (9), 1424–1439.

Sellers, P.J., Tucker, C.J., Collatz, G.J., et al., 1994. A global 1° by 1° NDVI data set for climate studies. Part 2: the generation of global fields of terrestrial biophysical parameters from the NDVI. Int. J. Remote Sens. 15 (17), 3519–3545.

Van der Tol, C., Berry, J., Campbell, P., Rascher, U., 2014. Models of fluorescence and photosynthesis for interpreting measurements of solar-induced chlorophyll fluorescence. J. Geo-phys. Res. Biogeosci. 119, 2312–2327.

Voigt, M., Guanter, L., Zhang, Y., Walther, S., Köhler, P., Jung, M., 2014. Global Analysis of the Relationship between Canopy-Scale Chlorophyll Fluorescence and GPP. In 5th International Workshop on Remote Sensing of Vegetation Fluorescence, April (pp. 22–24).

Wagle, P., Zhang, Y., Jin, C., Xiao, X., 2016. Comparison of solar-induced chlorophyll fluorescence, light-use efficiency, and process-

based GPP models in maize. Ecological applications 26 (4), 1211–1222.

Yang, H., Yang, X., Zhang, Y., Heskel, M. A., Lu, X., Munger, J. W., ... & Tang, J. (2017). Chlorophyll fluorescence tracks seasonal variations of photosynthesis from leaf to canopy in a temperate forest. Global change biology, 23(7), 2874–2886.

Yang, K., Ryu, Y., Dechant, B., Berry, J. A., Hwang, Y., Jiang, C., ... & Yang, X., 2018. Sun-induced chlorophyll fluorescence is more strongly related to absorbed light than to photosynthesis at half-hourly resolution in a rice paddy. Remote Sensing of Environment 216, 658–673.

Yang, P., van der Tol, C., 2018. Linking canopy scattering of far-red sun-induced chlorophyll fluorescence with reflectance. Remote Sens. Environ. 209, 456–467.

Yang, X., Tang, J., Mustard, J.F., Lee, J.-E., Rossini, M., Joiner, J., Munger, J.W., Kornfeld, A., Richardson, A.D., 2015. Solar-induced chlorophyll fluorescence correlates with canopy photosynthesis on diurnal and seasonal scales in a temperate deciduous forest. Geophys. Res. Lett. 42, 2977–2987.

Zarco-Tejada, P.J., Morales, A., Testi, L., Villalobos, F., 2013. Spatio-temporal patterns of chlorophyll fluorescence and physiological and structural indices acquired from hyperspectral imagery as compared with carbon fluxes measured with eddy covariance. Remote Sens. Environ. 133, 102–115.

Zarco-Tejada, P.J., González-Dugo, M.V., Fereres, E., 2016. Seasonal stability of chlorophyll fluorescence quantified from airborne hyperspectral imagery as an indicator of net photosynthesis in the context of precision agriculture. Remote Sensing of Environment 179, 89–103.

Zhang, Y., Guanter, L., Berry, J.A., van der Tol, C., Yang, X., Tang, J., Zhang, F., 2016a. Model-based analysis of the relationship between sun-induced chlorophyll fluorescence and gross primary production for remote sensing applications. Remote Sens. Environ. 187,145–155.

Zhang, Y., Xiao, X., Zhang, Y., Wolf, S., Zhou, S., Joiner, J., ... & Paul-Limoges, E., 2018a. On the relationship between sub-daily instantaneous and daily total gross primary production: Implications for interpreting satellite-based SIF retrievals. Remote sensing of environment 205, 276–289.

Zhang, Y., Joiner, J., Alemohammad, S. H., Zhou, S., Gentine, P., 2018b. A global spatially contiguous solar-induced fluorescence (CSIF) dataset using neural networks. Biogeosciences 15 (19), 5779–5800.

Zhang, Y., Wang, S., Liu, L., Ju, W., Zhu, X., 2017. ChinaSpec: a network of SIF observations to bridge flux measurements and remote sensing data. In Proceedings of the American Geophysical Union Fall Meeting, New Orleans, LA, USA, 11–15 December.

Zhang, Z., Zhang, Y., Zhang, Y., Chen, J. M., 2020. Correcting clear‐sky bias in gross primary production modeling from satellite solar‐induced chlorophyll fluorescence data. Journal of Geophysical Research: Biogeosciences, 125, e2020JG005822